DOI: 10.1002/adem.201080113

Superductile, Wavy Silica Nanostructures Inspired by Diatom Algae**

By *Andre P. Garcia, Nicola Pugno* and *Markus J. Buehler**

Biology implements intriguing structural design principles that allow for attractive mechanical properties—such as high strength, toughness, and extensibility despite being made of weak and brittle constituents, as observed in biomineralized structures. For example, diatom algae contain nanoporous hierarchical silicified shells, called frustules, which provide mechanical protection from predators and virus penetration. These frustules generally have a morphology resembling honeycombs within honeycombs, meshes, or wavy shapes, and are surprisingly tough when compared to bulk silica, which is one of the most brittle materials known. However, the reason for its extreme extensibility has not been explained from a molecular level upwards. By carrying out a series of molecular dynamics simulations with the first principles-based reactive force field ReaxFF, the mechanical response of the structures is elucidated and correlated with underlying deformation mechanisms. Specifically, it is shown that for wavy silica, unfolding mechanisms are achieved for increasing amplitude and allow for greater ductility of up to 270% strain. This mechanism is reminiscent to the uncoiling of hidden length from proteins that allows for enhanced energy dissipation capacity and, as a result, toughness. We report the development of an analytical continuum model that captures the results from atomistic simulations and can be used in multiscale models to bridge to larger scales. Our results demonstrate that tuning the geometric parameters of amplitude and width in wavy silica nanostructures are beneficial in improving the mechanical properties, including enhanced deformability, effectively overcoming the intrinsic shortcomings of the base material that features extreme brittleness.

The interest in nanoscale biomimetics and biologically inspired designs for structural and mechanical applications has significantly increased over the past few years. One reason for this lies in the apparent benefits that come from nanomaterials, including enhanced mechanical properties and multifunctionality. Yet, many of these materials are produced from generally expensive methods with possible toxic byproducts. But what if we could harness the benefits of nanomaterials through efficient and environmentally friendly mass production? Here, we use diatoms as a design paradigm to create novel nanoscale materials that encompass surprising mechanical properties, by utilizing a merger of structure and

[*] *A. P. Garcia, Prof. M. J. Buehler*
Laboratory for Atomistic and Molecular Mechanics
Department of Civil and Environmental Engineering 77
Massachusetts Ave. Room 1-235A&B,
Cambridge, MA (USA)
E-mail: mbuehler@MIT.EDU
A. P. Garcia, N. Pugno, Prof. M. J. Buehler
Laboratory of Bio-Inspired Nanomechanics ''Giuseppe Maria Pugno'', Department of Structural Engineering and Geotechnics, Politecnico di Torino Corso Duca degli Abruzzi 24, 10129, Torino (Italy)
A. P. Garcia, Prof. M. J. Buehler
Center for Computational Engineering 77 Massachusetts Ave., Cambridge, MA (USA)
N. Pugno
National Institute of Nuclear Physics, National Laboratories of Frascati Via E. Fermi 40, 00044, Frascati (Italy)
N. Pugno
National Institute of Metrological Research Strada delle Cacce 91, I-10135, Torino (Italy)

[**] *We acknowledge support from Army Research Office (grant number W9-11NNF-06-1029), the Gates Millennium Scholars Program, the National Science Foundation through a Graduate Research Fellowship, and a graduate research fellowship awarded by the Department of Civil and Environmental Engineering at the Massachusetts Institute of Technology. N. M. P. is supported by the Piemonte grant ''Metrology on a cellular and macromolecular scale for regenerative medicine''—METREGEN (2009-2012).*

RESEARCH ARTICLE

material in the development of a novel design paradigm to bridge the nano- to the macro-scale.

Although invisible to the naked eye, yet unconsciously implemented in structures throughout human history, diatoms have served as a silent backbone to human civilization and play a role in cement manufacturing, carbon sequestration, water filters, and oil production.[1–7] The answer to their broad ranging importance lies at the nanoscale, where diatoms are micrometer sized algae with silicified, porous shells. Generally, these pores and surrounding walls have nanometer to micrometer dimensions and serve to protect the organism and sustain multiple biological functions. Examples of mechanical protection include preventing virus penetration, crushing from some predator's mandibles, or digestion.[8–10] A particularly interesting colonial diatom is *Ellerbeckia arenaria* because they live in waterfalls and are thus able to resist significant and continual mechanical stress and deformation. These colonies are also able to elastically stretch up to a remarkable level of about 33%.[11,12] Two possible reasons for this extreme mechanical response are the intrinsically shaped cell wall and the organic coating, called mucilage, surrounding the cell wall surface. In this paper, we focus on the corrugated, wavy shape found along the sides of *E. arenaria* [see Fig. 1(a)], and test our hypothesis that this particular shape is essential to providing flexibility while combining high strength and toughness.

Interestingly, many other biological systems such as collagen[13–15] or intermediate filaments[16–19] also share the hierarchical structural makeup with those of diatoms, presenting a universal design paradigm of biological materials that has been shown a key element to turn weakness to strength.[20–22] The reason for biology's universal implementation of hierarchical structures might lie in the intricate interplay between the triumvirate of process, structure, and property, which are all contingent upon the requirement of survival of biological species, such as defense under extreme conditions, and under severe limitations of material quality and quantity. Because of the unique mechanical properties of diatoms, a second look at harnessing biomineralization is necessary to incorporate the governing role of genetics in the formation of structures. Some first steps have already been taken by genetic sequencing of certain diatoms, allowing a better understanding at which proteins are responsible for the intricate nanoscale shapes seen on the frustules.[23] As the primary material that makes up diatom shells is also the most abundant material of Earth's crust, silica, this serves as a cornerstone in the efficient mass production of lightweight functional materials, devises, and machines derived from diatoms.[24] The ability to self assemble diatoms onto a surface through inkjet printing is an important discovery that will help facilitate large-scale functionalization of diatom silica in industry.[25]

Previous studies on frustules have discovered a broad range of mechanical properties that correlate with specific sections of the diatom. For example, atomic force microscopy (AFM) nanoindentation performed on the three hierarchical layers making up the frustule, revealed elastic moduli ranging

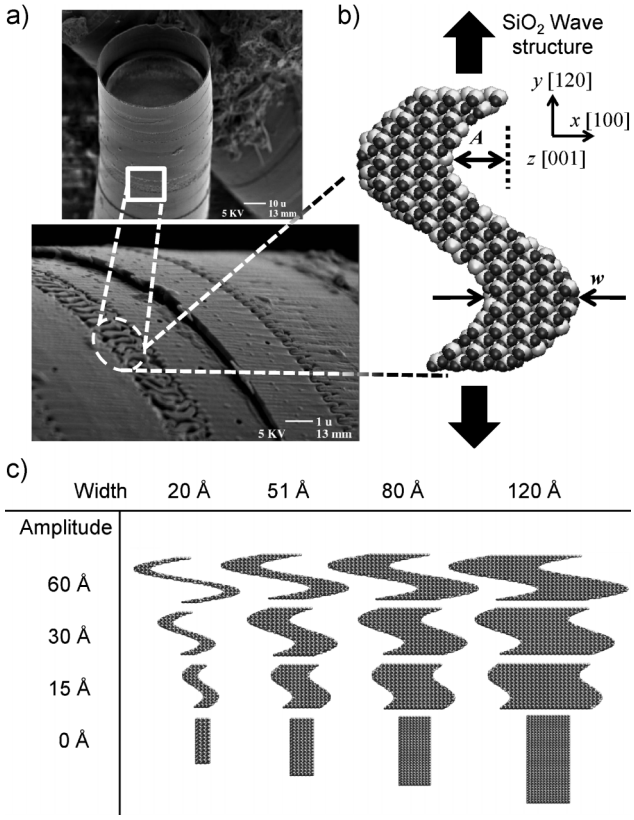

Fig. 1. Panel (a): A colonial diatom, E. arenaria, lives in waterfalls and contains girdle bands with intricate patterns. Specifically, a wave shape can be seen, which might be an important contribution to the elastic response of approximately 33%, as observed through AFM experiments.[11] Panel (b): Initial geometry of a bioinspired silica structure used in our simulations, illustrating the wall width and amplitude (w and A, definitions indicated in the structure). Panel (c): Initial geometry of all wave structures considered here, illustrating the range of variation in amplitude and width. Images reprinted from ref. [11 Gebeshuber et al. Journal of Nanoscience and Nanotechnology, Copyright (c) 2005 (permission pending).

between 3.40 and 15.61 GPa.[26] Another AFM study revealed the region outside the curved ends of the raphe fissure reached a stiffness between 100 and 300 GPa.[27] Possible reasons for this variability in mechanical response lie in the unique geometry of each layer, including the porosity, pore distance, and pore size. Other studies[28] performed on frustules using a glass needle observed a high elastic response. They also constructed a finite element model to simulate the effect from applied pressure on several regions along the diatom's side, similar to that of a predator's mandible bite. A homogenous stress distribution and stress deflections were observed, indicating that structural morphology plays a critical role in the structural integrity of the diatom. Earlier work by the authors used full-atomistic simulations to describe the behavior of diatom inspired nanoporous silicon and silica, revealing that size scaling enables significant tailorability of toughness, stress, and ductility.[29,30] Recently, the authors established a size-dependent brittle-to-ductile transition in nanoporous silica structures, and discovered that structures showing plastic yielding also show large toughness improvement over bulk silica.[31] Here, we explore a unique diatom cell wall morphology that allows for extreme ductility

which is achieved through unfolding mechanisms and hidden length.

Integrated silicon circuits have been manufactured with a wavy structural layout and 1.7 μm thickness, and can be elongated up to 10%.[32] Other studies revealed highly ductile amorphous silica nanowires, by using a taper-drawing process. Ranging from 20 nm in diameter and with highly smooth surfaces, the nanowires achieve extreme flexibility such that rope-like twists and spiral coils are realized.[33] However, even though these manmade nanostructures offer attractive mechanical properties, they are generally unfeasible for mass production due to complex and expensive manufacturing. For this reason, a second look at harnessing biomineralization is necessary. The first steps have already been taken by genetic sequencing of certain diatoms, allowing a better understanding at what proteins are responsible for the intricate nanoscale shapes seen on the frustules.[23] As the ability to create these magnificent structures increases, so does the necessity to understand the fundamental mechanical properties they endow. In light of this, we focus on the silica nano-wave structures found in *E. arenaria* and use first principles based ReaxFF atomistic simulations to probe the mechanical response and failure mechanisms (details see Materials and Methods).

Results and Discussion

We present our analysis on the effect of altering the amplitude and wall width on the mechanical properties of the silica wave structures [see Fig. 1(c) for the two geometries considered]. As shown in Figure 1(c), the wall width w and amplitude A, which range from 20 to 120 Å, and 0 to 60 Å, respectively. These structures resemble those found in some diatoms, such as *E. arenaria*. The stress strain response for all structures is shown in Figure 2. Here we observe a maximum strain of 270% for the structures with largest amplitude of 60 Å and a width of 51 Å. Interestingly, the initial modulus of these structures is roughly ten times lower than those with lower amplitude. For structures with largest width and lowest amplitude, the greatest modulus and maximum stress are reached: $E = 14.4$ GPa and $\sigma_{max} = 5$ GPa. The general trend is for decreasing failure strain, and greater modulus and maximum stress as the wall width is increased and the amplitude is lowered.

Next, we analyze the effect of altering the wall width and amplitude on the toughness, ductility, maximum stress, and modulus, as seen in Figure 3. The toughest response is seen for amplitudes below 30 Å and greater than 5 Å. It is important to note that these structures are defect free, and thus the upper limit on toughness can diverge from experimental ones. Ductility is highest, reaching ≈270%, for amplitudes of 60 Å, and 51 Å $\leq w \leq$ 80 Å. The largest maximum stress is found for 0 Å $\leq A \leq$ 15 Å of and 80 Å $\leq w \leq$ 120 Å. Toughness versus modulus is compared in Figure 3(c), showing that they are both positively correlated for decreasing amplitude. However, the increased toughness and modulus comes at the expense of ductility. The structure with greatest toughness of

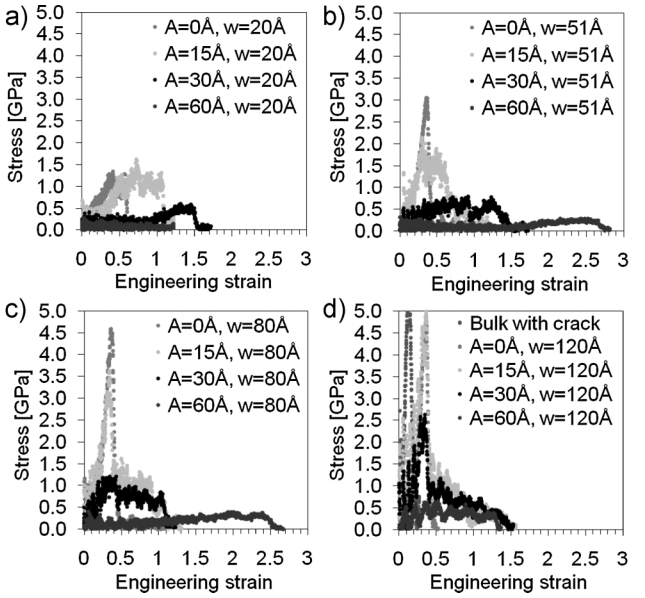

Fig. 2. Stress–strain graph of silica wave strictures, for $w = 20$ Å panel (a), $w = 51$ Å panel (b), $w = 80$ Å panel (c), and $w = 120$ Å panel (d). Panel (a): The structures of lowest width, 20 Å, resist a maximum stress of 1.5 GPa, seen in $A = 20$ Å. For $A = 60$ Å, $w = 20$ Å, the structure fails immediately upon loading. In $A = 30$ Å, $w = 20$ Å, the structure unfolds and straightens, thus allowing for steep increase and plateau in stress at 100% strain. Panel (b): The structures with amplitudes of 15 and 30 Å increase in brittleness when the wall width is increased. However, for $A = 30$ Å the ductility is drastically increased to 283% strain. The gradual increase in stress indicates subtle unfolding and eventual straightening of the structure. Panel (c): As wall widths are increased to 80 Å the maximum stress rises for all structures, but also fails sooner than structures with smaller widths. Panel (d): The highest stress is observed, reaching 5 GPa for $A = 15$ Å, $w = 120$ Å. However, brittleness increases dramatically and the unfolding mechanisms is no longer observed for $A = 60$ Å, $w = 120$ Å, which fails at 130% strain. Failure mechanisms characteristic of the most brittle structures, such as $A = 15$ Å, $w = 120$ Å, are crack and shear, along with void formations that coalesce with other voids until the structure is no longer intact. Bulk silica has many defects which allow for its brittle nature. To test this we perform a simulation of periodic bulk silica with a penny shaped crack 5 Å wide and 120 Å long that extends through 120 Å of silica, and that failed at 12% strain and reached a maximum stress of 5.3 GPa.

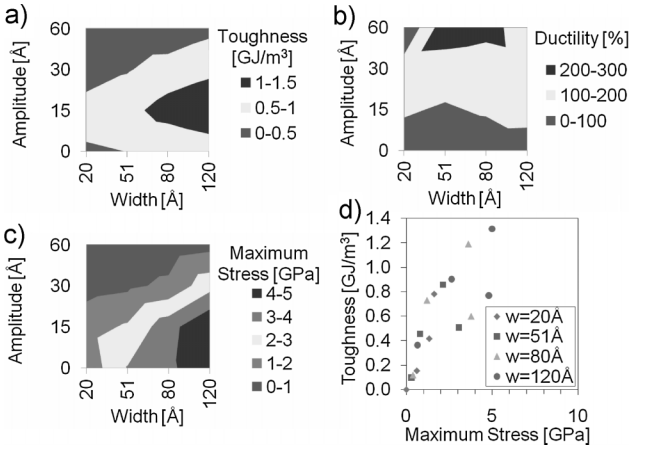

Fig. 3. Panel (a): Toughness map, showing that greatest toughness is achieved for structure with $A = 15$ Å, $w = 120$ Å. Panel (b): Ductility map. Structures with greatest ductility have the highest amplitude, reaching up to 283%. However, as the amplitude becomes 0–15 Å, ductility is generally below 100%. Panel (c): Maximum stress map, showing that structures with lowest amplitude and large width, such as $A = 15$ Å, $w = 120$ Å, reach a stress up to 5 GPa. Panel (d): Nonlinear relationship between modulus and maximum stress. The structure with greatest toughness is $A = 15$ Å, $w = 120$ Å.

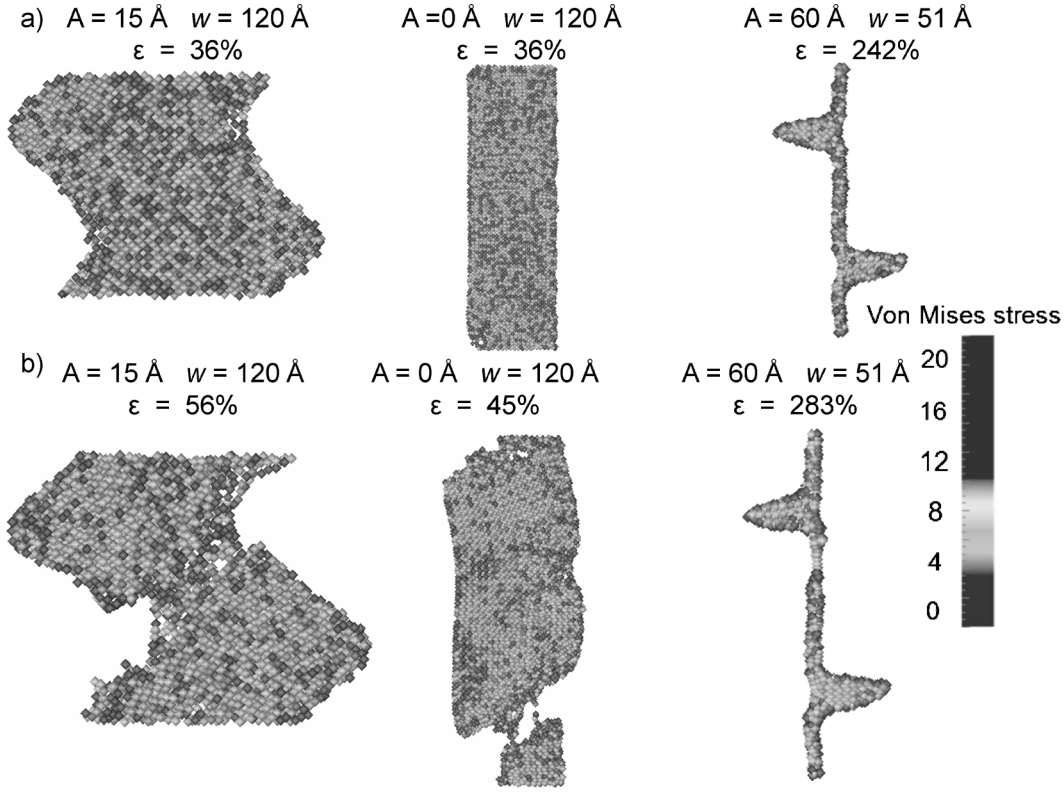

Fig. 4. Von Mises stress field for structures at maximum stress, panel (a), and at failure, panel (b) (stress in GPa). Panel (a): The structure with $A = 15$ Å, $w = 120$ Å contains a significant portion of the stress to form a straight line, and lower stress near the curved regions. For $A = 0$ Å, $w = 120$ Å the stress is relatively homogeneous, with highest stress on the surface. For $A = 60$ Å, $w = 51$ Å high stress is concentrated along the extended, vertical ligaments. Panel (b): High stress is observed near the failure process zone for the structure with $A = 15$ Å, $w = 120$ Å. The structure forms voids near the corner and shearing occurs next. For $A = 0$ Å, $w = 120$ Å, failure is mainly crack formation, while unfolding and beading is observed for $A = 0$ Å, $w = 120$ Å.

1.3 GJ m^{-3} corresponds with a relatively low ductility of ≈ 50%. The observed deformation mechanisms are closely linked to the mechanical response of each structure.

In Figure 4 we compare the Von Mises stress fields of three structures and the corresponding deformation mechanisms during failure which correlate with three distinct mechanical responses: high toughness, high ductility, and high stress. The structure with highest toughness is shown in Figure 4(a), and contains a significant portion of the stress to form a straight line, and lower stress near the curved regions. As failure occurs, cracking initiates near the corners and propagates in a diagonal shearing fashion. Void formation dictates the path of cracking, while the shearing effect breaks off the outermost surface of the voids in a sequential manner, similar to a beading mechanism. For structures with highest ductility, the deformation path is unfolding and finally beading. The unfolding mechanism encompasses the straightening of the central, or core structure, while the wave peaks remain in the initial conformation and open up slightly. Rotation of the core region is enhanced by single void formation near the corners. The core region is defined as the area bounded by the inner peaks of the wave. For structures with maximum stress, the deformation mechanism is mainly cracking, with very little shear deformation.

Next, we map the regions of best performance—ductility, toughness, and maximum stress—and its relationship with the amplitude and width, as seen in Figure 5. For structures with high amplitude and low width, greatest ductility is achieved; whereas low amplitude and high width is yields the greatest strength. The structures of highest toughness have a width and amplitude bounded by the regions of highest ductility and stress. Interestingly, it is a balance of both geometric parameters (A and w) and a combination of

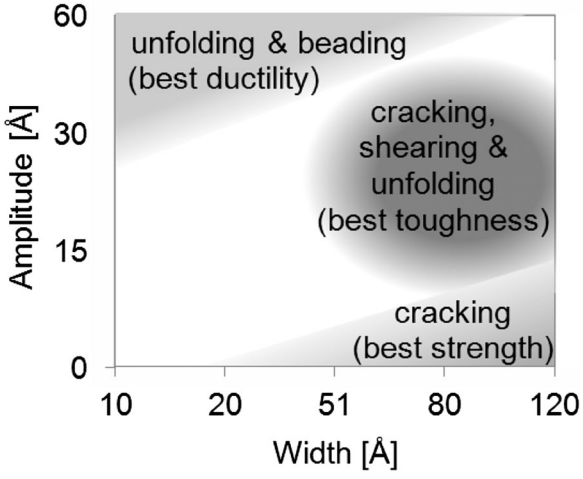

Fig. 5. Material performance map, showing the regions where optimum toughness, ductility, and strength are located with respect to width and amplitude.

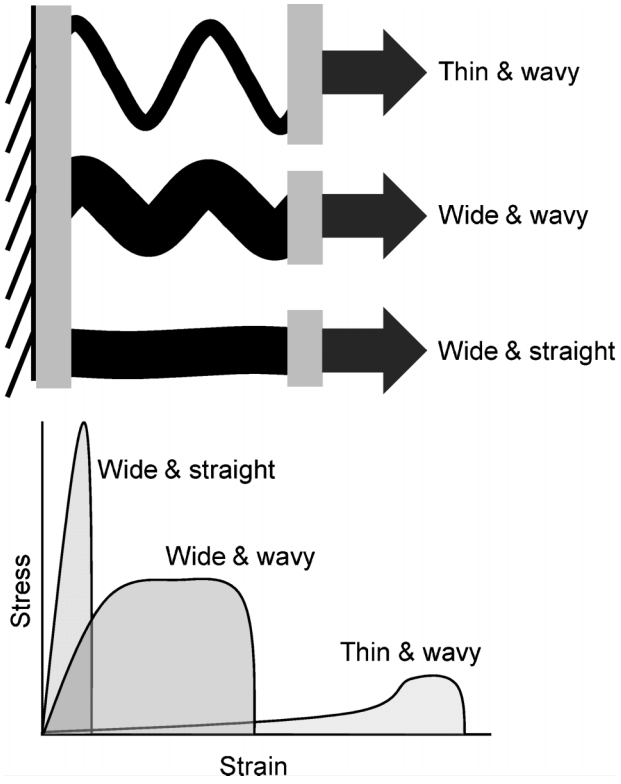

Fig. 6. Schematic of stress–strain response for tensile deformation of different morphologies of silica wavy structures, summarizing the results from atomistic simulations. Thin and wavy structures provide greatest ductility, while wide and straight structures provide high stress at the cost of ductility. However, when combining wavy and wide morphologies, a significant toughness can be achieved.

deformation mechanisms (unfolding, shearing, and cracking) which allow for greatest toughness. Furthermore, this concept of geometric effects on the stress–strain behavior are displayed in Figure 6.

The behavior observed from atomistic simulation as summarized in Figure 6, can be deeply understood and quantified by a self-consistent hyper-elastic-plastic model of the wavy silica nanostructure. Referring to Figure 6, the thin/wide behavior is characterized by small/large ρ and w, whereas the wavy/straight behavior by large/small $a_y \approx a_0$ (with respect to the fixed initial wavelength λ_0). Thus, according to Equations (18), (21), and (22), we expect for: ''thin & wavy'': elasticity with small Young modulus, large strain and hyper-elasticity, plasticity at small stress (and large strain); ''wide & wavy'': elasticity with intermediate Young modulus, plasticity at intermediate stress (hyper-elastic regime virtually activated at a strain similar to that of the previous case and thus preceded by the plastic collapse); ''wide & straight'': elasticity with large Young modulus (comparable to that intrinsic of the material, thus no hyper-elasticity), fracture (that must precede plasticity, virtually arising only at very large stress); These analytical predictions exactly correspond to the scenario that emerges from our atomistic simulations, as we quantitatively compare in Table 1 and Figure 7. Note that for a ''thin & straight'' structure all the configurations are allowed: elasticity with

Table 1. Comparison between numerical simulations versus theoretical predictions (no best fit parameter is used in the comparison; the intrinsic material properties are assumed to be identical to those derived from the pure in-silico tensile test, i.e., the ''wide & straight'' case).

	Thin & wavy	Wide & wavy	Wide & straight
A [Å]	30.00	30.00	0.00
w [Å]	20.00	80.00	120.00
λ [Å]	63.50	63.50	–
E_{in} [GPa]	0.01 vs. 0.49	3.25 vs. 2.20	12.33
E_{fin} [GPa]	0.81 vs. <12.33[a]	–	–
ε_{y-in}	1.04 vs. 1.22	0.33 vs. 0.63	0.36
ε_{y-fin}	1.45 vs. <11.98[b]	1.02 vs. < 3.91[b]	–
σ_y [GPa]	0.60 vs. 0.60	1.20 vs. 1.38	4.83

[a] This upper bound Young's modulus is the intrinsic one of the material; obtained from the wide & straight structure;
[b] these upper bound strains predictions assume the final rectilinear geometrical configuration.

small/large Young modulus, possible presence of the hyperelastic regime, fracture or even plasticity, suggesting a rather complex behavior as a result of these mechanisms.

An analogy to protein structures can be drawn, wherein sacrificial bonds and hidden lengths are responsible for enhanced toughness.[20,34,35] These sacrificial bonds are weaker than the carbon backbone, but stronger than van der Waals or hydrogen bonds, and allow for saw-tooth shape force-extension curves. Sulfate bonds are a great example of sacrificial bonds in systems containing DOPA, a common amino acid found in biological adhesives. As each sacrificial bond breaks, energy is released in the form of heat and a regional unfolding, or uncoiling of a hidden length segment, occurs. This process is repeated until all the sacrificial bonds are broken and the structure is completely unfolded. Only then will the carbon backbone break, resulting in the highest peak of stress. The interplay of multiple failure zones and deformation mechanisms is strikingly similar to those found in the silica wave structures. A link is made between the sacrificial bonds found in proteins, and the shearing mechanism found in the silica wave. The catastrophic carbon backbone failure is also analogous to cracking in a silica system. When integrating these multiple mechanisms, a universal concept of enhancing toughness is achieved.

Conclusions

In summary, here we have investigated the fundamental impact of wave-shaped geometries on the mechanical response of silica, by utilizing an atomistic simulation approach based on the first principles reactive force field ReaxFF and combined with a theoretical continuum model. The overall agreement between continuum theory and simulation results suggests that continuum approaches are powerful tools in rationalizing and extending (e.g., toward larger length-scales) the results of more detailed atomistic simulations. Specifically, we are able to demonstrate a drastic increase of the ductility of silica, up to 270%, by increasing the

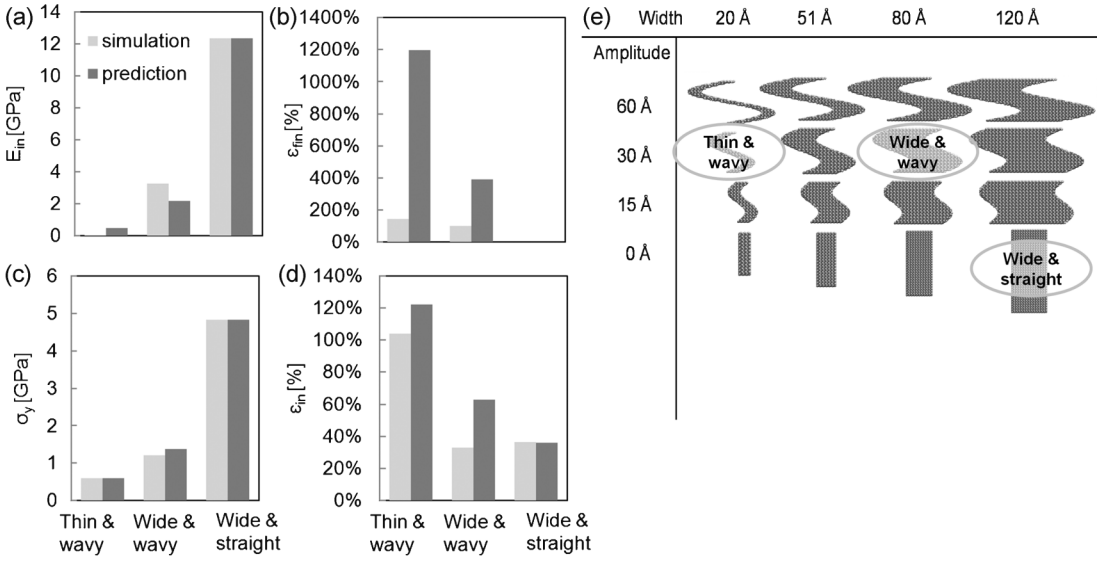

Fig. 7. Comparison between simulation and continuum theory prediction, with data as shown in Table 1. The predictions of the continuum theory are based on deducing the Young's modulus and yielding strength from the wide & straight structure (see details at the end of the Theoretical Hyper-elastic-plastic Model section) and subsequently considering solely variations of the geometry, without fitting parameters. The overall agreement between continuum theory and simulation results suggests that continuum approaches are powerful tools in rationalizing and extending (e.g. for larger size-scales) the results of more detailed atomistic simulations. Panel (a): Initial Young's modulus. Panel (b): Final strain, indicating the strain at which failure occurs after the plastic regime has passed. For the ''thin & wavy'' and ''wide & wavy'' cases the values do not agree well, indicating that the molecular simulation provides a better approximation as the continuum theory can no longer describe associated deformation mechanisms. Panel (c): Stress at which yielding occurs. Panel (d): Initial strain, indicating the onset of yielding. Panel (e): Initial geometry of all wave structures in the study, indicating the three structures that are considered for comparison between simulation and theoretical prediction.

amplitude to 60 Å and maintaining the width at 51 Å. This is achieved by unfolding mechanisms and straightening of the structure, similar to the uncoiling of hidden length from a convoluted protein. The structures with greatest toughness, reaching values of up to 1.3 GJ·m^{-3}, have a 15 Å amplitude and a 120 Å width. And finally, the greatest strength is obtained from straight and widest, $w = 120$ Å, structures; noting, however, that the structures investigated here are defect free.

Several challenges remain in the form of fabricating and perhaps more accurately modeling these structures. For example, biomineralization from self assembling proteins which guide silica precipitation has been studied.[36–39] However, the ability to synthesize complex and hierarchical structures as studied here still remains challenging. The recent determination of certain diatom genetic sequences will further the understanding of accurately controlling and fabricating silica structures. In terms of modeling these systems, a key consideration is the effect of surface reconstruction and termination on the mechanical properties. Although it is expected that our ReaxFF-based approach can capture surface reconstruction in principle,[40] it is computationally expensive to capture this due to associated time-scale and system size, and was thus not observed in our simulations. When exposed to natural environments, silica surfaces generally become terminated with hydrogen atoms after exposure to moisture. Results have been obtained in previous studies of silica nanorod deformation in the presence of water using semi-empirical quantum mechanics methods,[41] where the authors concluded that strained siloxane (Si–O–Si) bonds are attacked by water which results in lower stress and lower failure strain of the silica nanorod, compared to a dry silica nanorod. These are critical issues that should be explored in future investigations.

Other future research could be geared toward atomistic simulations on the deformation and failure of different morphologies found in diatom species. Moreover, mineralized structures are found in many other biological systems, such as deep see sponges,[42] which could be studied using a similar molecular approach. Common features in sponges are hierarchical mineralized structures along with imbedded organic material; whereas in diatom shells, a large portion of the organic material is found in the form of an organic mucilage layer covering the outer diatom. Another important step is reaching a greater convergence between actual diatom frustules and those modeled. Key challenges are reaching greater size scales, incorporating organic material, amorphization, and surface termination. The size scale issue can be generally overcome with coarse graining, or utilizing massive supercomputers on the order of thousands of CPUs with ReaxFF. With larger systems, more complex shapes can be modeled, such as incorporating different shapes throughout the z axis. Perhaps a more complicated challenge is the addition of organic material, such as proteins, within the silica structure, in order to elucidate the impact on the mechanical properties of the composite structure. The existing ReaxFF force field that can be used to model both organics and silica is limited to glyoxal, and does not encompass nitrogen bonds, an element frequently found in many organic structures, such as collagen protein.[43] Once adequate force fields are developed and validated, proteins such as silaffins and collagen could be added to the silica phase and their interactions investigated. As previous studies have mentioned, proteins within diatoms

are found in their adhesives and enable self-assembling.[44] Amorphization of silica is another critical concept that should be explored, since it could affect the mechanical properties and is also found in diatoms. Another avenue for further research is surface termination, as it occurs when silica is exposed to water, and does affect the mechanical response of silica structures. Future simulations of surface terminated structures can encompass larger systems in order to more fully capture the effect at different length scales.

The ability to transform multiple mechanical properties, such as toughness, strength, and ductility, is extremely important when looking into future applications of nanoscale materials. Altering the mechanical properties of one of the most brittle and abundant minerals on earth, silica, allows a new window of opportunity for humanity to create new applications and reinvent materials once thought to be impossible. The transferability of the concept allowing for massive transformation of mechanical responses, such as brittle to ductile or weak to tough, through geometric alterations at the nanoscale, is another profound discovery that may unleash a new paradigm in the way materials are designed and applied. Indeed, the culmination of materials design is to maintain environmental sustainability, infrastructure superiority, multifunctional capacity, and economic feasibility. Nanoscale materials, implemented through design and fabrication concepts found in diatom algae, hold the promise of providing these advantages.

Materials and Methods

Force Field

Atomistic simulations are a powerful tool to capture complex nanoscale phenomena and underlying mechanisms. To that end, we use the ReaxFF force field, which is derived solely from first principles quantum mechanical (QM) calculations.[45] ReaxFF has been shown to accurately describe the behavior of a variety of materials, including bond breaking and formation process of organics (C, O, H, N), metals (Cu, Al, Mg, Ni, Pt), semiconductors (Si), mixed Si–O systems, and silica–water interfaces.[45–50] The ability of ReaxFF to describe the large-deformation and bond breaking behavior aspect is critical to describe the properties of materials under extreme conditions, and in particular at large deformation and during failure. Specifically, a well tested and validated ReaxFF force field is available for silica.[47] We use the ReaxFF force field implemented in the large-scale atomic/molecular massively parallel simulator (LAMMPS).[51]

Model Geometry

We consider a structural design composed of alpha-quartz crystals. The structure is a foil or infinitely tall thin wall with varying amplitude and width, resembling a wave, as seen in Figure 1(b). Since the simulation box is periodic, the foil structure can be thought of an array of waves with a spacing equivalent to the peak-to-peak amplitude. The z axis has no free surface, and the structure can be described as infinitely tall. Figure 1(c) shows the geometries considered here. All wave structures have an equivalent wavelength of 63.5 Å. The only parameter varied here is the wall width w and amplitude A, which range from 20 to 120 Å, and 0 to 60 Å, respectively [see Fig. 1(c)]. The number of atoms varies from ≈ 650 to 7000 for the smallest to the largest width silica systems. For the wave structures, the largest simulation cell has dimensions of 177 Å × 63.5 Å × 8.5 Å in the x-, y-, and z-direction.

Simulation Approach

All structures are equilibrated under the canonical ensemble at 300 K for a time of 10 ps and then loaded under uniaxial strain loading along the [1 2 0] direction as shown in Figure 1(b), at a strain rate of 1×10^{10} s^{-1} at 300 K. The system has periodic boundary conditions in all three directions and the temperature is controlled by the Berendsen thermostat.[52] Deformation is applied by uniaxially increasing the size of the periodic simulation cell in the loading direction only, while keeping all other dimensions of the simulation cell constant. We use a time step of 0.2 fs. The initial, unstrained silica structure is shown in Figure 1(c). Aside from the variations in the geometry, all simulations are carried out under identical conditions, enabling us to perform a systematic comparison.

Mechanical Analysis

We calculate the virial stress[48] by

$$\sigma_{IJ} = \frac{\sum_k^N m_k v_{kI} v_{kj}}{V} + \frac{\sum_k^N r_{k_I} \cdot f_{k_J}}{V}, \quad (1)$$

where N, m, v, r, f, and V are the are the number of atoms, mass of atom, velocity, position, force, and total system volume, respectively. In order to improve image clarity, we only show the stress values associated with silicon atoms when plotting the stress fields. Generally, the oxygen atoms have a much broader stress distribution than silicon atoms, and therefore the stress patterns are difficult to observe if both atom types are shown.

The engineering strain is defined as:

$$\varepsilon = \frac{\Delta L_y}{L_y}, \quad (2)$$

where L_y is the initial length of the specimen, and ΔL_y is the change in the length along the deformation direction (which is the y-coordinate). The stress–strain curve is then used to determine the elastic modulus, E, where $\sigma = \sigma_{22}$ (tensile stress in the loading direction)

$$E = \frac{\partial \sigma}{\partial \varepsilon} \approx \frac{\Delta \sigma}{\Delta \varepsilon}. \quad (3)$$

Once the stress–strain curves are determined, their integral is taken in order to determine the toughness

$$E_V = \int_0^{\varepsilon_f} \sigma(\varepsilon) \mathrm{d}\varepsilon, \quad (4)$$

where E_v and ε_f are the energy per unit volume and strain at failure, respectively. A higher toughness indicates a greater ability of the material to absorb energy due to stresses before failure (resulting for instance in a larger fracture process zone). The Von Mises stress σ_v is calculated as

$$\sigma_v = \sqrt{\frac{(\sigma_{xx}-\sigma_{yy})^2+(\sigma_{yy}-\sigma_{zz})^2+(\sigma_{xx}-\sigma_{zz})^2+6\left(\sigma_{xy}^2+\sigma_{yz}^2+\sigma_{zx}^2\right)}{2}}, \tag{5}$$

where σ_{II} ($I = x,y,z$) are the normal components of the stress tensor, and σ_{xy}, σ_{yz}, and σ_{zx} are the shear components of the stress tensor. We apply the above expression [Eq. (5)] for the Von Mises stress in plotting the atomic stresses during maximum and failure stresses.

Theoretical Hyper-elastic-plastic Model

To model the behavior observed in atomistic simulation we use a self-consistent hyper-elastic-plastic model of the wavy silica nanostructure. We describe its geometry by

$$x = a\sin 2\pi\frac{y}{\lambda} \tag{6}$$

where a is the amplitude, y the longitudinal coordinate, and λ is the wavelength [$a = A + w/2$, see Fig. 1(b)]. If two self-equilibrated forces F are applied along y at the ends of the structure, its stored elastic energy per unit length will be

$$\frac{dL}{ds} = \frac{1}{2}\left(\frac{N^2}{ES}+\frac{M^2}{GI}\right) \tag{7}$$

where N is the axial load, M the bending moment, E and G the material Young and shear modulus, S the cross-sectional surface area, and I is the moment of inertia (along z) of the structure. Noting that $M = Fx$, $N = F\cos\alpha$, with $\tan\alpha = dx/dy$, and that $\rho = \sqrt{I/S}$ (for a rectangular beam $\rho = w/\sqrt{12}$) is the radius of inertia, the stored energy per unit length becomes:

$$\frac{dL}{ds} = \frac{1}{2}\frac{F^2}{ES}\left(\cos^2\alpha(y)+\frac{x^2(y)}{\rho^2}\right) \tag{8}$$

with

$$\cos\alpha(y) = \frac{1}{\sqrt{1+\left(\frac{dx(y)}{dy}\right)^2}} \tag{9}$$

Since $ds = dy/\cos\alpha$, we can derive the elastic energy cumulated in one wavelength, as:

$$L = \frac{1}{2}\frac{F^2}{EA}\int_0^\lambda\left[\cos\alpha(y)+\frac{x^2(y)}{\rho^2\cos\alpha(y)}\right]dy \tag{10}$$

Thus, the equivalent Young modulus can be derived by comparison with

$$L = \frac{1}{2}\frac{F^2}{E_{eq}A}\ell \tag{11}$$

where

$$\ell = \int_\ell ds = \int_0^\lambda \frac{dy}{\cos\alpha(y)} \tag{12}$$

as

$$E_{eq}(a,\lambda) = \frac{\int_0^\lambda \frac{1}{\cos\alpha(y)}dy}{\int_0^\lambda\left[\cos\alpha(y)+\frac{x^2(y)}{\rho^2\cos\alpha(y)}\right]dy}E \tag{13}$$

A self-consistent non-linear constitutive law can be described by a Young modulus $E_{eq}(a,\lambda)$ in which a and λ are the actual values imposed by a nominal strain $\varepsilon = (\lambda-\lambda_0)/\lambda_0$, where subscript 0 refer to the unstrained initial configuration; thus, $\lambda(\varepsilon) = (1+\varepsilon)\lambda_0$. The strained sinusoidal geometry, described by the function $a(\varepsilon)$ (in addition to $\lambda(\varepsilon)$), can be derived neglecting the axial with respect to the flexural compliance, i.e., imposing

$$\ell = \ell_0 \tag{14}$$

from which we can obtain $a(\varepsilon)$. The sinusoid will reach the straight configuration ($a = 0$) under a nominal strain:

$$\varepsilon^* = \frac{\ell_0-\lambda_0}{\lambda_0} \tag{15}$$

Thus, we could finally derive the non-linear self-consistent Young modulus of the sinusoidal structure $E_{eq}(a_0,\lambda_0,\varepsilon \le \varepsilon^*)$ introducing $a(\varepsilon)$ and $\lambda(\varepsilon)$ into $E_{eq}(a,\lambda)$; for $\varepsilon \ge \varepsilon^*$, $E_{eq}(a_0,\lambda_0, \varepsilon \ge \varepsilon^*) = E$. The outlined procedure requires the solutions of elliptical integrals as well as of the root of a nonlinear equation, thus it can be obtained only numerically. On the other hand, we can easily find the asymptotic solution for slightly deformed configurations, i.e., for small values of the parameter a/λ. We accordingly deduce:

$$E_{eq}(a << \lambda,\lambda) = \frac{1-\pi^2\frac{a^2}{\lambda^2}}{1-\pi^2\frac{a^2}{\lambda^2}+\frac{a^2}{\rho^2}\left(\frac{1}{2}+\frac{3}{4}\pi^2\frac{a^2}{\lambda^2}\right)}E \tag{16}$$

$$\ell = \lambda\left(1+\frac{\pi^2a^2}{\lambda^2}\right) \tag{17}$$

$$\varepsilon^* = \frac{\pi^2a_0^2}{\lambda_0^2} \tag{18}$$

$$a(\varepsilon) = \sqrt{a_0^2(1+\varepsilon)-\frac{\lambda_0^2}{\pi}(1+\varepsilon)\varepsilon} \tag{19}$$

and finally

$$E_{\mathrm{eq}}(a_0 << \lambda_0, \lambda_0, \varepsilon) = \begin{cases} \dfrac{1-\pi^2\dfrac{a_0^2}{\lambda_0^2}}{1-\pi^2\dfrac{a_0^2}{\lambda_0^2}+\dfrac{a_0^2(1+\varepsilon)-\frac{\lambda_0^2}{\pi}(1+\varepsilon)\varepsilon}{\rho^2}\left(\dfrac{1}{2}+\dfrac{3}{4}\pi^2\dfrac{a_0^2}{\lambda_0^2}\right)}E, & \varepsilon \le \varepsilon^* \\ E\varepsilon \ge \varepsilon^* \end{cases} \tag{20}$$

Equation (17) predicts, in the stress versus strain curve, an initial elastic Young modulus of

$$E_{\mathrm{eq}} \approx E \Big/ \left(1+\frac{1}{2}\frac{a_0^2}{\rho^2}\right), \tag{21}$$

and then a hyper-elastic regime with $E_{\mathrm{eq}} \to E$. Moreover, plastic hinges could form at the points of maximum stresses, i.e., at $x = \mp a$. This could happen, if fracture does not prevail, for an applied stress (equating the plastic moment of a rectangular beam to the maximum moment $\approx Fa$, and defining $\sigma = F/S$)

$$\sigma_y \approx \frac{w\sigma_P}{4a_y} \tag{22}$$

where σ_P is the material yield strength, σ_y the structural yield strength, and a_y is the value of a at yielding.

In order to compare this analytical model with our atomistic simulations, we start deducing the intrinsic material properties of silica, E and σ_P from the ''wide & straight'' structure computational analysis (see Table 1); then, from Equation (21 and 22), we compare our predictions of σ_y and $E_{\mathrm{in}} \approx E_{\mathrm{eq}}$ for the other structures (see Table 1) without any further parameter fitting. We deduce also $\varepsilon_{y-\mathrm{in}} \approx \sigma_y/E_{\mathrm{in}}$; the upperbounds of the final strains, corresponding to the final straight configuration, which are predicted according to Equation (18), i.e., $\varepsilon_{y-\mathrm{fin}} < \varepsilon^*$. An upper bound of the Young modulus is also fixed for all the structures as equal to the intrinsic material Young modulus E. The comparison shows a relevant agreement apart from the initial value of the Young modulus for the ''thin & wavy'' structure, probably due to the difficulty of defining it in the computation, as a consequence of observed structural initial rearrangements.

Received: October 11, 2010
Final Version: December 21, 2010
Published online: March 29, 2011

[1] D. Losic, J. G. Mitchell, N. H. Voelcker, *Adv. Mater.* **2009**, *21*, 1.
[2] D. Fragoulis, M. G. Stamatakis, D. Papageorgiou, E. Chaniotakis, *Cem. Concr. Compos.* **2005**, *27*, 205.
[3] S. Chatterji, *Cem. Concr. Res.* **1978**, *8*, 461.
[4] W. Fenical, *Plants: the potentials for extracting protein, medicines, and other useful chemicals: workshop proceedings*. **1983**, U.S. Government Printing Office: Washington, D.C. p. 147.
[5] J. T. Allen, L. Brown, R. Sanders, C. Mark Moore, A. Mustard, S. Fielding, M. Lucas, M. Rixen, G. Savidge, S. Henson, D. Mayor, *Nature* **2005**, *437*, 728.
[6] E. Litchman, C. A. Klausmeier, K. Yoshiyama, *Proc. Natl. Acad. Sci.* **2009**, *106*, 2665.
[7] T. V. Ramachandra, D. M. Mahapatra, B. Karthick, R. Gordon, *Indus. Eng. Chem. Res.* **2009**, *48*, 8769.
[8] J. A. Raven, A. M. Waite, *Tansley Rev.* **2003**, *162*, 45.
[9] C. E. Hamm, V. Smetacek, *Armor: why, when, and how, in Evolution of Primary Producers in the Sea* (Eds: P. G. Falkowski, A. H. Knoll), Elsevier, Boston **2007**, pp. 311.
[10] S. W. Fowler, N. S. Fisher, *Deep Sea Res.* **1983**, *39*, 963.
[11] I. C. Gebeshuber, H. Stachelberger, M. Drack, *J. Nanosci. Nanotechnol.* **2005**, *5*, 79.
[12] I. C. Gebeshuber, J. H. Kindt, J. B. Thompson, Y. Del Amo, H. Stachelberger, M. Brzezinski, G. D. Stucky, D. E. Morse, P. K. Hansma, *J. Microsc. -Oxford* **2004**, *214*, 101.
[13] P. Fratzl, R. Weinkamer, *Prog. Mater. Sci.* **2007**, *52*, 1263.
[14] P. Fratzl, *Collagen: Structure and Mechanics*, Springer, New York **2008**.
[15] H. S. Gupta, J. Seto, W. Wagermaier, P. Zaslansky, P. Boesecke, P. Fratzl, *Proc. Natl. Acad. Sci. U. S. A.* **2006**, *103*, 17741.
[16] Z. Qin, L. Kreplak, M. J. Buehler, *PLoS One* **2009**, *4*, e7294.
[17] L. Kreplak, D. Fudge, *Bioessays* **2007**, *29*, 26.
[18] C. Guzman, S. Jeney, L. Kreplak, S. Kasas, A. J. Kulik, U. Aebi, L. Forro, *J. Mol. Biol.* **2006**, *360*, 623.
[19] S. V. Strelkov, L. Kreplak, H. Herrmann, U. Aebi, *Intermed. Filament Cytoskeleton* **2004**, *78*, 25.
[20] M. J. Buehler, Y. C. Yung, *Nat. Mater.* **2009**, *8*, 175.
[21] M. J. Buehler, *Nat. Nano* **2010**, *5*, 172.
[22] M. J. Buehler, *Nano Today* **2010**, *5*, 379.
[23] E. V. Armbrust, J. A. Berges, C. Bowler, B. R. Green, D. Martinez, N. H. Putnam, S. Zhou, A. E. Allen, K. E. Apt, M. Bechner, M. A. Brzezinski, B. K. Chaal, A. Chiovitti, A. K. Davis, M. S. Demarest, J. C. Detter, T. Glavina, D. Goodstein, M. Z. Hadi, U. Hellsten, M. Hildebrand, B. D. Jenkins, J. Jurka, V. V. Kapitonov, N. Kroger, W. W. Y. Lau, T. W. Lane, F. W. Larimer, J. C. Lippmeier, S. Lucas, M. Medina, A. Montsant, M. Obornik, M. S. Parker, B. Palenik, G. J. Pazour, P. M. Richardson, T. A. Rynearson, M. A. Saito, D. C. Schwartz, K. Thamatrakoln, K. Valentin, A. Vardi, F. P. Wilkerson, D. S. Rokhsar, *Science* **2004**, *306*, 79.
[24] S. R. Taylor, *Geochim. Cosmochim. Acta* **1964**, *28*, 1273.
[25] W. Wang, T. Gutu, D. K. Gale, J. Jiao, G. L. Rorrer, C-h. Chang, *J. Am. Chem. Soc.* **2009**, *131*(12), 4178.
[26] D. Losic, K. Short, J. G. Mitchell, R. Lal, N. H. Voelcker, *Langmuir*, **2007**, *23*(9), 5014.
[27] N. Almqvist, Y. Delamo, B. L. Smith, N. H. Thomson, Å. Bartholdson, R. Lal, M. Brzezinski, P. K. Hansma, *J. Microsc.* **2001**, *202*(3), 518.

[28] C. E. Hamm, R. Merkel, O. Springer, P. Jurkojc, C. Maier, K. Prechtel, V. Smetacek, *Nature* **2003**, *421*(6925), 841.
[29] A. P. Garcia, M. J. Buehler, *Comput. Mater. Sci.* **2010**, *48*(2), 303.
[30] A. P. Garcia, D. Sen, M. J. Buehler, *Metall. Mater. Trans. A.* accepted for publication, **2011**.
[31] D. Sen, A. P. Garcia, M. J. Buehler, *J. Nanomech. Micromech.* in submission.
[32] D.-H. Kim, J.-H. Ahn, W. M. Choi, H.-S. Kim, T.-H. Kim, J. Song, Y. Y. Huang, Z. Liu, C. Lu, J. A. Rogers, *Science* **2008**, *320*(5875), 507.
[33] L. Tong, J. Lou, Z. Ye, G. T. Svacha, E. Mazur, *Nanotechnology* **2005**, *16*(9), 1445.
[34] G. E. Fantner, E. Oroudjev, G. Schitter, L. S. Golde, P. Thurner, M. M. Finch, P. Turner, T. Gutsmann, D. E. Morse, H. Hansma, P. K. Hansma, *Biophys. J.* **2006**, *90*(4), 1411.
[35] B. L. Smith, T. E. Schaffer, M. Viani, J. B. Thompson, N. A. Frederick, J. Kindt, A. Belcher, G. D. Stucky, D. E. Morse, P. K. Hansma, *Nature* **1999**, *399*(6738), 761.
[36] N. Kroger, N. Poulsen, *Annu. Rev. Genet.* **2008**, *42*, 83.
[37] N. Kroger, *Curr. Opin. Chem. Biol.* **2007**, *11*(6), 662.
[38] M. Sumper, G. Lehmann, *ChemBioChem* **2006**, *7*(9), 1419.
[39] M. Sumper, E. Brunner, *Adv. Funct. Mater.* **2006**, *16*(1), 17.
[40] D. Raymand, A. C. T. van Duin, M. Baudin, K. Hermansson, *Surf. Sci.* **2008**, *602*(5), 1020.
[41] E. Silva, J. Li, D. Liao, S. Subramanian, T. Zhu, S. Yip, *J. Comput. -Aided Mater. Des.* **2006**, *13*(1), 135.
[42] J. Aizenberg, J. C. Weaver, M. S. Thanawala, V. C. Sundar, D. E. Morse, P. Fratzl, *Science* **2005**, *309*(5732), 275.
[43] R. Z. Kramer, J. Bella, B. Brodsky, H. M. Berman, *J. Mol. Biol.* **2001**, *311*(1), 131.
[44] T. M. Dugdale, R. Dagastine, A. Chiovitti, R. Wetherbee, *Biophys. J.* **2006**, *90*(8), 2987.
[45] A. C. Tv. Duin, S. Dasgupta, F. Lorant, W. A. Goddard, *J. Phys. Chem. A* **2001**, *105*, 9396.
[46] M. J. Buehler, A. C. Tv. Duin, W. A. Goddard, *Phys. Rev. Lett.* **2006**, *96*(9), 095505.
[47] A. C. Tv. Duin, A. Strachan, S. Stewman, Q. Zhang, X. Xu, W. A. Goddard, *J. Phys. Chem. A* **2003**, *107*, 3803.
[48] J. A. Zimmerman, E. B. W, III J. J. Hoyt, R. E. Jones, P. A. Klein, D. J. Bammann, *Modell. Simul. Mater. Sci. Eng.* **2004**, *12*(4), S319.
[49] M. J. Buehler, H. Tang, A. C. T. van Duin, W. A. Goddard, *Phys. Rev. Lett.* **2007**, *99*(16), 165502.
[50] J. C. Fogarty, H. M. Aktulga, A. Y. Grama, A. C. T. van Duin, S. A. Pandit, *J. Chem. Phys.* **2010**, *132*(17), 174704.
[51] S. J. Plimpton, *J. Comp. Phys.* **1995**, *117*, 1.
[52] H. J. C. Berendsen, J. P. M. Postma, W. F. van Gunsteren, A. DiNola, J. R. Haak, *J. Chem. Phys.* **1984**, *81*(8), 3684.

